

Computational Prediction and Experimental Realization of Earth-Abundant Transparent Conducting Oxide Ga-Doped ZnSb₂O₆

Adam J. Jackson,[‡] Benjamin J. Parrett,[‡] Joe Willis,[‡] Alex M. Ganose, W. W. Winnie Leung, Yuhuan Liu, Benjamin A. D. Williamson, Timur K. Kim, Moritz Hoesch, Larissa S. I. Veiga, Raman Kalra, Jens Neu, Charles A. Schmuttenmaer, Tien-Lin Lee, Anna Regoutz, Tung-Chun Lee, Tim D. Veal, Robert G. Palgrave, Robin Perry,* and David O. Scanlon*

Cite This: *ACS Energy Lett.* 2022, 7, 3807–3816

Read Online

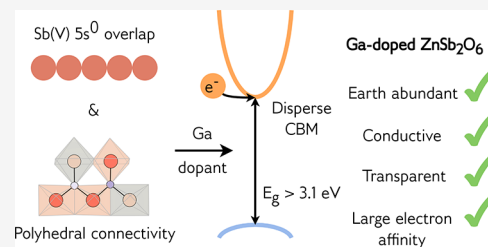
ACCESS |

Metrics & More

Article Recommendations

Supporting Information

ABSTRACT: Transparent conducting oxides have become ubiquitous in modern optoelectronics. However, the number of oxides that are transparent to visible light and have the metallic-like conductivity necessary for applications is limited to a handful of systems that have been known for the past 40 years. In this work, we use hybrid density functional theory and defect chemistry analysis to demonstrate that tri-rutile zinc antimonate, ZnSb₂O₆, is an ideal transparent conducting oxide and to identify gallium as the optimal dopant to yield high conductivity and transparency. To validate our computational predictions, we have synthesized both powder samples and single crystals of Ga-doped ZnSb₂O₆ which conclusively show behavior consistent with a degenerate transparent conducting oxide. This study demonstrates the possibility of a family of Sb(V)-containing oxides for transparent conducting oxide and power electronics applications.



Transparent conducting oxides (TCOs) are an essential component of modern photovoltaic and display screen technologies. Thin-film Sn-doped In₂O₃ (ITO) displays the superior optoelectronic properties among the industrially used TCOs; it has been reported to possess resistivities as low as $8 \times 10^{-5} \Omega\text{-cm}$, mobilities that exceed $50 \text{ cm}^2 \text{ V}^{-1} \text{ s}^{-1}$, and carrier concentrations on the order of $1 \times 10^{21} \text{ cm}^{-3}$, all while retaining over 90% transparency to visible light.¹ The more earth-abundant TCOs, such as F-doped SnO₂ (FTO)² or Al-doped ZnO (AZO),³ display mobilities and conductivities below those of ITO, which limits their application in display screen technologies. However, it is undesirable to continue to use ITO for large-area applications such as in photovoltaics, despite recent improvements in the efficiency of indium-based TCOs via innovative doping (Mo and Ce),^{4–6} due to the expense and scarcity of indium. Therefore, there is a drive to try to increase the performance of the known earth-abundant TCOs^{7,8} or, more unusually, to discover new TCOs. The last “new” materials demonstrated to be TCOs were the thin-film correlated metals SrVO₃ and CaVO₃ in 2015 and single-crystal La-doped BaSnO₃ in 2012.^{9,10}

In terms of materials design, the common trend in the majority of the effective n-type TCOs is the presence of post-

transition-metal cations with the electronic structure $(n-1)d^{10}ns^0np^0$. In these materials, the valence s orbitals of the cation hybridize with antibonding oxygen $2p$ states, yielding conduction bands with low electron effective masses.¹¹ Indeed, the majority of the cations in the industrially relevant TCOs are limited to groups 12, 13, and 14 of the periodic table.

In an early investigation of ternary oxides, Shannon et al. noted that edge-sharing Cd²⁺, In³⁺, and Sn⁴⁺ octahedra were a feature of common transparent conductors.¹² Mizoguchi and Woodward built on this in 2004, investigating the necessity for edge-sharing octahedral connectivity when designing n-type TCOs.¹³ They found that edge-sharing is not a prerequisite, and corner-sharing can also provide excellent dispersion of the conduction band, such as in BaSnO₃.¹⁰ Interestingly, they identified some ternary oxides containing Sb(V) and Bi(V) which displayed reasonable curvature of the conduction band minimum (CBM),¹³ including tri-rutile zinc antimonate,

Received: August 30, 2022

Accepted: October 5, 2022

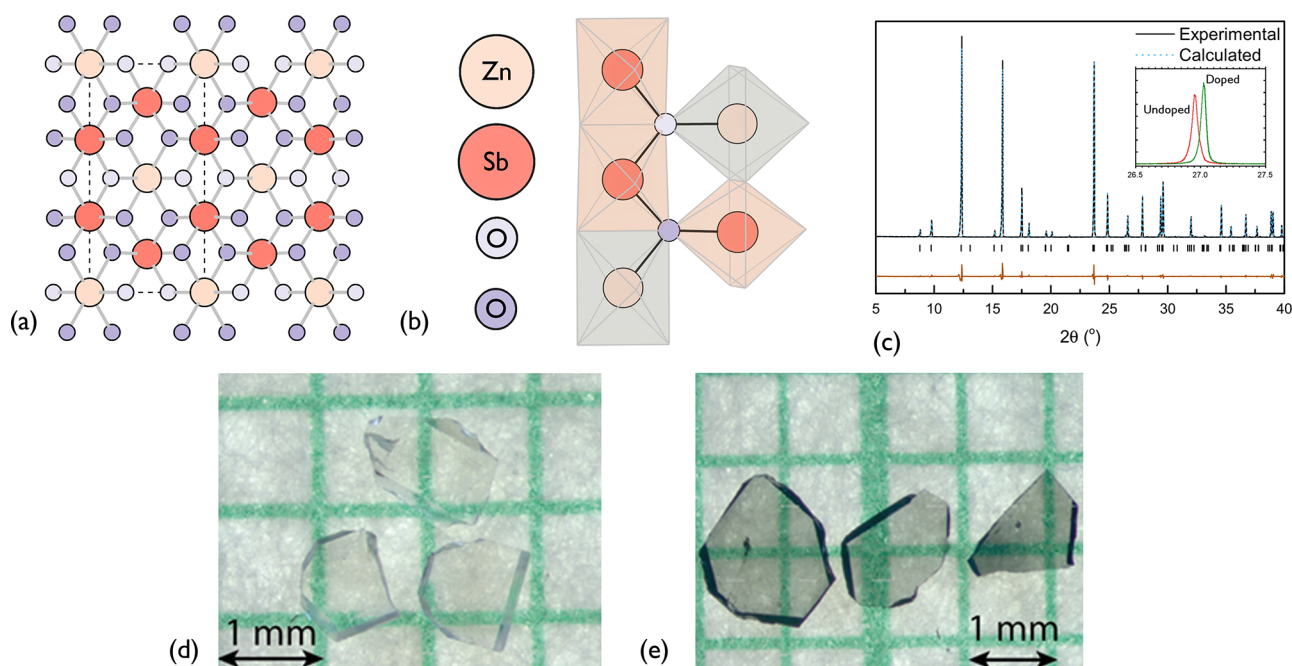


Figure 1. (a) View along the *a*-axis of the crystal structure of ZnSb₂O₆. (b) Octahedral connectivity in ZnSb₂O₆, viewed from a slight offset of the *a*-axis, which is edge-sharing in the *c*-direction and corner-sharing in the *a*- and *b*-directions. (c) Powder and simulated X-ray diffraction patterns for ZnSb₂O₆. The dashed line indicates Rietveld refinement for *P*₄₂/*mnm* tri-rutile structure; the difference between fit and data is shown below the peak positions. The inset shows the typical shift in an XRD peak upon Ga-doping. (d) Undoped ZnSb₂O₆ single crystals and (e) Ga-doped ZnSb₂O₆ single crystals. All crystal structures were visualized using VESTA.²²

ZnSb₂O₆. It should be noted that group 15 cations in their highest oxidation states possess the same $(n - 1)d^{10}ns^0np^0$ electronic structure as the cations in the common, successful TCOs.

In 2014, a computational screening study from Hautier et al. also proposed ZnSb₂O₆ as a potential transparent conductor, in particular noting its low electron effective mass and earth-abundant, nontoxic composition.¹⁴ Several other stibnates and germanates were highlighted, but none was followed up with a defect chemistry analysis showing n-type dopability. On the few occasions that ZnSb₂O₆ has been synthesized experimentally, transparent conducting behavior has not been observed. Kikuchi et al. investigated it as a TCO and thermoelectric in 2005,¹⁵ but it was only produced as a powder, and little data on the optoelectronic properties were published. Thick films of crystalline ZnSb₂O₆ have been deposited for gas-sensing applications via dip-coating and vapor-phase oxidation methods,^{16,17} although no assessment of their transparent conducting potential has been reported. Spin-coating of a nanoparticle precursor followed by high-temperature annealing was found to result in transparent insulating ZnSb₂O₆ thin films, which deteriorated in terms of both transparency and crystallinity upon F-doping.¹⁸ Finally, Li et al. briefly investigated ZnSb₂O₆ as a potential anode for Li battery technology.¹⁹ Synthesis of high-quality thin films or single crystals of ZnSb₂O₆ has not been realized, and its full potential as a transparent conductor has yet to be assessed.

In this work, we investigated the crystal and electronic structure of ZnSb₂O₆ with hybrid density functional theory, and validated this description with quasi-particle self-consistent GW theory (Green's function, *G*, with a screened Coulomb interaction, *W*). A full intrinsic defect analysis was performed that showed that, when nominally undoped, ZnSb₂O₆ does not fulfill the Mott criterion for metallic-like conductivity. We then

considered three extrinsic dopants, and demonstrated that Ga is the optimum electron donor in ZnSb₂O₆. Using this knowledge, we successfully grew powder and single-crystal samples of Ga-doped ZnSb₂O₆, which displayed a low absorption coefficient (88 cm⁻¹) in the visible range, electron mobility up to 49 cm² V⁻¹ s⁻¹, conductivity up to 1890 S cm⁻¹, carrier concentrations on the order of 2 × 10²⁰ cm⁻³, and a Haacke figure of merit comparable with that of polycrystalline ITO. We calculated the electron affinity of ZnSb₂O₆ to be nearly 1 eV larger than that of currently available transparent electrodes, offering much needed diversity when considering the band alignment of potential contact layers in devices. Ga-doped ZnSb₂O₆ displays all the indicators of a high-performance transparent conductor, with the added bonus of being comprised of earth-abundant elements: Zn and Sb are several orders of magnitude cheaper per kilogram than In, while Ga is required in only very small amounts.²⁰ This study stands as an important proof-of-concept for Sb(V)-based TCO design, and invites the development of thin-film deposition to further investigate the optoelectronic properties of ZnSb₂O₆ and to prepare it for use in devices and commercial applications.

Crystal Structure. ZnSb₂O₆ crystallizes in a tri-rutile structure, belonging to the *P*₄₂/*mnm* space group, as shown in Figure 1a. The structure consists of ZnO₆ and SbO₆ edge-sharing octahedra in the order ZnO₆–SbO₆–SbO₆ along the *c*-axis, with corner-sharing octahedra present throughout the *a*–*b* planes (Figure 1a,b). The unit cell is tetragonal, and a summary of the fundamental parameters is provided in Table S1 for a range of exchange correlation functionals and experiments. The powder X-ray diffraction (XRD) results show an excellent fit to the *P*₄₂/*mnm* space group, as can be seen in Figure 1c, and the calculated PBE0 lattice parameters are in good agreement with room-temperature XRD results.

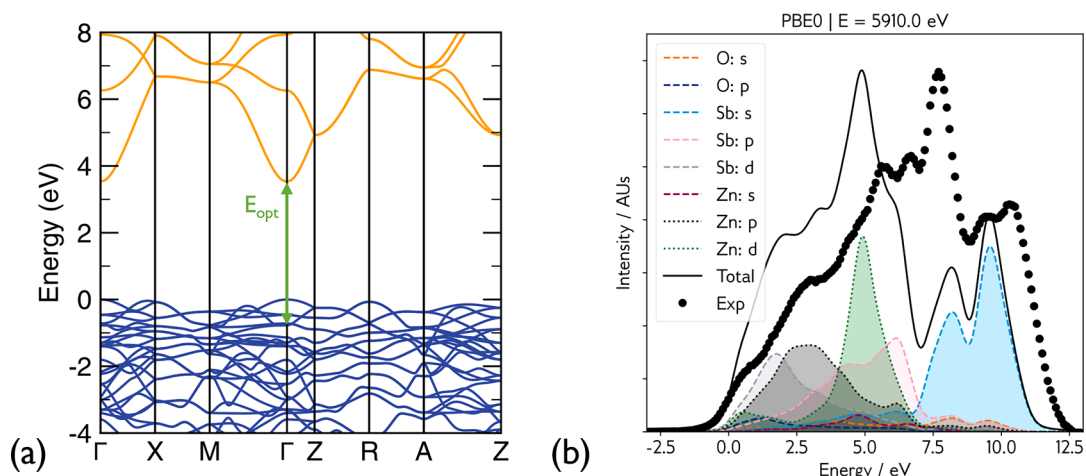


Figure 2. (a) Electronic band structure of ZnSb_2O_6 computed using the PBE0 functional. (b) Simulated valence band spectra using the PBE0 functional, weighted by the photoionization cross sections for a photon energy of 5.91 keV, and broadened by a Gaussian of 0.6 eV and a Lorentzian of 0.2 eV. Plotted in black is the HAXPES experimental valence band spectrum of a nominally undoped single crystal, collected at a photon energy of 5.91 keV. Both spectra are normalized to the peak maxima.

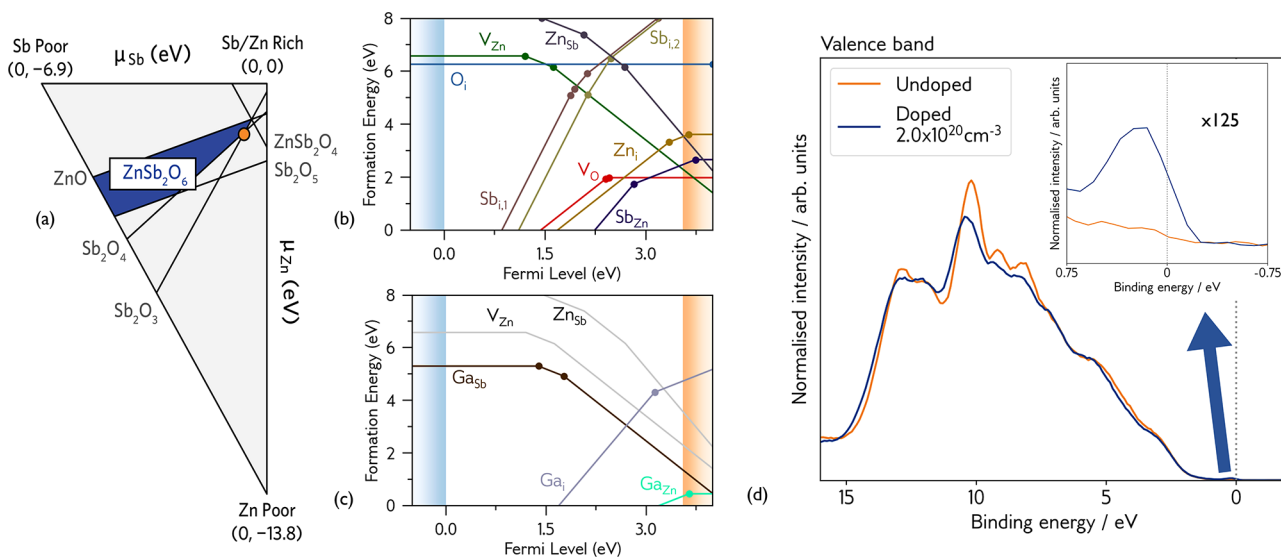


Figure 3. (a) Thermodynamic stability region of ZnSb_2O_6 , calculated using CPLAP.³¹ The orange marker denotes the most n-type growth conditions, the chemical potential limits at which the defect formation energies in this work are reported. (b) Intrinsic defect transition level diagram of ZnSb_2O_6 . (c) Extrinsic defect transition level diagram of ZnSb_2O_6 . (d) Experimental HAXPES valence band spectra of undoped and Ga-doped ZnSb_2O_6 , normalized to area under the curve. The inset shows a $\times 125$ magnification at the Fermi level, denoted by a dotted gray line. For transition level diagrams, blue and orange shaded regions denote the valence and conduction bands, respectively. Each colored line represents a different defect, and the gradient of that line denotes the charge state. Filled circles represent transition levels, where two charge states are in thermodynamic equilibrium. Calculated and plotted using AIDE. For V_{O} , O_{i} , F_{O} , Zn_{i} , and Ga_{i} , only the lower energy of the two non-equivalent defect sites is plotted. The gray lines in (c) show the native p-type acceptor defects V_{Zn} and Zn_{Sb} .

We note the PBEsol lattice parameters are slightly overestimated, which is typical of the generalized gradient approximation (GGA) implementation in DFT.²¹

Doping with Ga causes a systematic shift in the Bragg peaks to higher angles compared to those of undoped samples, illustrated in the inset of Figure 1c, indicating a shrinkage in cell size. This observation is consistent with substituting Ga with Zn in an octahedral environment, as Ga has a smaller ionic radius (0.62 Å) compared to Zn (0.74 Å).²³ The unit cell volumes shift from 201.78 Å³ to 201.48 Å³ after 6% Ga doping, extracted by Rietveld refinement using the GSAS-II software.²⁴ These observations are consistent with a solid solution of gallium replacing zinc in the tri-rutile structure, with no detectable phase separation. Optical images of our transparent

undoped and Ga-doped single crystals are shown in Figure 1d,e, approximately 1 mm² in area and polished to a thickness of around 150 μm.

Electronic Structure. We begin with a discussion of the electronic structure, arguably the most decisive indicator of a prospective transparent conductor. The electronic band structure of ZnSb_2O_6 was calculated using the PBE0 functional and is displayed in Figure 2a. A direct band gap of 3.54 eV at Γ is observed, with relatively high dispersion at the CBM. The electron effective mass in the $\Gamma \rightarrow X$ and $\Gamma \rightarrow M$ directions is $0.27m_e$, and improves further along $\Gamma \rightarrow Z$ (in the c -direction) to $0.22m_e$. The high dispersion originates from the broad overlap of Sb 5s orbitals, which are the main contributors to the CBM density of states, with Zn and O s states.

Qualitatively, the conduction band shape is in good agreement with previous GGA-DFT calculations, while the hybrid functional corrects for the systematic underestimation of the band gap,¹⁴ which we note is competitive with state-of-the-art TCOs In₂O₃, SnO₂, ZnO, and BaSnO₃.^{2,7,8,25} Figure S6 shows the band structure computed with hQSGW theory, which shows a small (3%) decrease in the direct band gap to 3.41 eV, with the electron effective masses unchanged. Ultimately, the PBE0 description is sufficient, accurately describing the nature of the band gap compared to the next level of theory, and is used subsequently for defect calculations. The transition from valence band maximum (VBM) to CBM is symmetry forbidden, and the first allowed transition occurs from states around 0.7 eV below the VBM (similar to the case in In₂O₃),²⁶ as denoted by the green arrow in Figure 2a. This is discussed in greater detail in the Optical Properties section.

Simulated and experimental photoelectron spectra of the valence band of undoped ZnSb₂O₆ are shown in Figure 2b, plotted using Galore.^{27,28} The simulated spectrum was obtained from the PBE0 density-of-states calculation, where the orbital contributions were weighted with tabulated photoionization cross sections and broadened with Gaussian and Lorentzian functions to reproduce the experimental line shapes. The spectra were approximately aligned to the Fermi level. The key valence band features in Figure 2b are in agreement: an initial onset mainly comprised of Zn 3*d*, Sb 4*d*, and O 2*p* states followed by a sharp peak assigned to Zn 3*d* states. However, the position of this peak is under-bound by approximately 3 eV. The under-binding of transition metal *d* states with hybrid DFT is well documented and has been observed in other well-known TCOs, such as the Zn 3*d* states in ZnO and Sn 4*d* states in SnO₂.^{29,30}

Defect Chemistry. While the electronic structure of ZnSb₂O₆ is a promising indicator of high TCO performance, it is the defect chemistry that will ultimately control the electrical properties of the system. Degenerate conductivity is achieved when the charge carrier concentration exceeds the Mott criterion:^{32–35}

$$n_{\text{Mott}} > \left(\frac{0.26}{a_0} \right)^3$$

$$\text{where } a_0 = \frac{4\pi\epsilon_0\epsilon_\infty\hbar^2}{m^*e^2} \text{ and } \frac{1}{m^*} = \frac{1}{m_e^*} + \frac{1}{m_h^*} \quad (1)$$

which for ZnSb₂O₆ is $2.6 \times 10^{18} \text{ cm}^{-3}$, where a_0 is the effective Bohr radius ($1.89 \times 10^{-9} \text{ m}$), ϵ_0 is the calculated static dielectric constant (7.74), and m^* is the reduced effective mass ($1.97 \times 10^{-31} \text{ kg}$).

We first identify the thermodynamic stability region (blue) of ZnSb₂O₆ with respect to its competing phases in Figure 3a. This gives an insight into which synthesis conditions are most appropriate for growing n-type ZnSb₂O₆ (denoted by the orange circle), and provides the chemical potentials required for calculating the defect formation energies under those synthesis conditions (equation S1). The transition level diagram for intrinsic defects, namely zinc, antimony, and oxygen vacancies (V_{Zn} , V_{Sb} , and V_{O}), cation substitutions (Zn_{Sb} and Sb_{Zn}), and various interstitial sites (Zn_i , Sb_i , and O_i), is calculated and displayed in Figure 3b for the most n-type chemical potential limits, corresponding to an oxygen-poor, metal-rich environment.

The intrinsic defect chemistry does not support degenerate n-type behavior. V_{O} acts as a deep donor defect, in line with the behavior observed in established TCOs such as In₂O₃, SnO₂, and ZnO (CdO being the notable exception),^{5,8,36–38} and is discussed in greater detail in the SI. The Sb_{Zn} substitution is the next lowest energy species, but it is charge-compensated by V_{Zn} (see Figure S5) just below the CBM, pinning the Fermi level in the gap. We predict the position of the Fermi level and charge carrier concentrations through a self-consistent Fermi level (SCFL) analysis. The synthesis temperature of our ZnSb₂O₆ single crystals is $\sim 1400 \text{ K}$, and by fixing the defect concentrations present at this temperature and recalculating the SCFL at room temperature, we can predict room-temperature experimental charge carrier concentrations. Undoped ZnSb₂O₆ is predicted to have $3.1 \times 10^{16} \text{ cm}^{-3}$ charge carriers (significantly below the Mott criterion), with the SCFL 0.13 eV below the conduction band edge, precluding undoped ZnSb₂O₆ from metallic-like conductivity. From experiment, we measure $5.0 \times 10^{17} \text{ cm}^{-3}$ carriers in undoped crystals, around an order of magnitude more than predicted, and low conductivity (around 2 S/cm). The slight deviation in carrier concentration measured in the crystals is likely due to adventitious H-doping during synthesis, as well as trace amounts of other impurities that could contribute electrons (such as Cl from the carrier gas), but is in qualitative agreement with the SCFL analysis—i.e., when nominally undoped, ZnSb₂O₆ does not display metallic conductivity.

Next, we considered a strategy for electron donation in ZnSb₂O₆. Knowing that the Sb *s* states mainly comprise the conduction pathway, we primarily targeted the Zn and O sites for substitution to leave the conduction band unperturbed. Ruling out some of the larger 3+ cations, as they would cause large lattice disruption, Al, Ga (for Zn substitution), and F (for O substitution) were selected as potential dopants for driving the Fermi level into the conduction band and realizing degenerate conductivity.

The transition level diagram for Ga-doping is shown in Figure 3c, while the Al and F data is presented in Figure S8. We find that Ga_{Zn} and Al_{Zn} are low-energy donors, with formation energies of 0.45 eV and 0.58 eV in their neutral charge states, respectively. In both cases, the dopant interstitial defects are rather high in energy (around 5 eV at the CBM), and are charge-compensated by their respective dopant substitutions onto the Sb site. F_{O} anion substitutions have higher formation energies of 1.38 eV and 1.46 eV for the inequivalent oxygen sites, while the F interstitials do not donate electrons to the conduction band. Crucially, we find that the native p-type defects, V_{Zn} and Zn_{Sb} , are too high in energy to charge-compensate Ga_{Zn} , Al_{Zn} , and F_{O} . We complete the same SCFL analysis as before for each case, and find that Ga has a predicted room-temperature charge carrier concentration of $3.4 \times 10^{19} \text{ cm}^{-3}$ and a SCFL of 3.69 eV (0.15 eV above the CBM), thereby predicting degenerate conductivity. For Al and F, the predicted charge carrier concentrations are $3.2 \times 10^{19} \text{ cm}^{-3}$ and $7.2 \times 10^{18} \text{ cm}^{-3}$, with the SCFL sitting above the CBM in both cases. However, Al-doping of ZnSb₂O₆ was unsuccessful experimentally, with various Al precursors not responding well to the CVT growth method, and F-doping was not attempted due to the lower predicted achievable carrier concentration, so Ga emerged as the optimal dopant. Experimentally, we record carrier concentrations of $8.9 \times 10^{19} \text{ cm}^{-3}$, $2.0 \times 10^{20} \text{ cm}^{-3}$, and $2.4 \times 10^{20} \text{ cm}^{-3}$ in three single

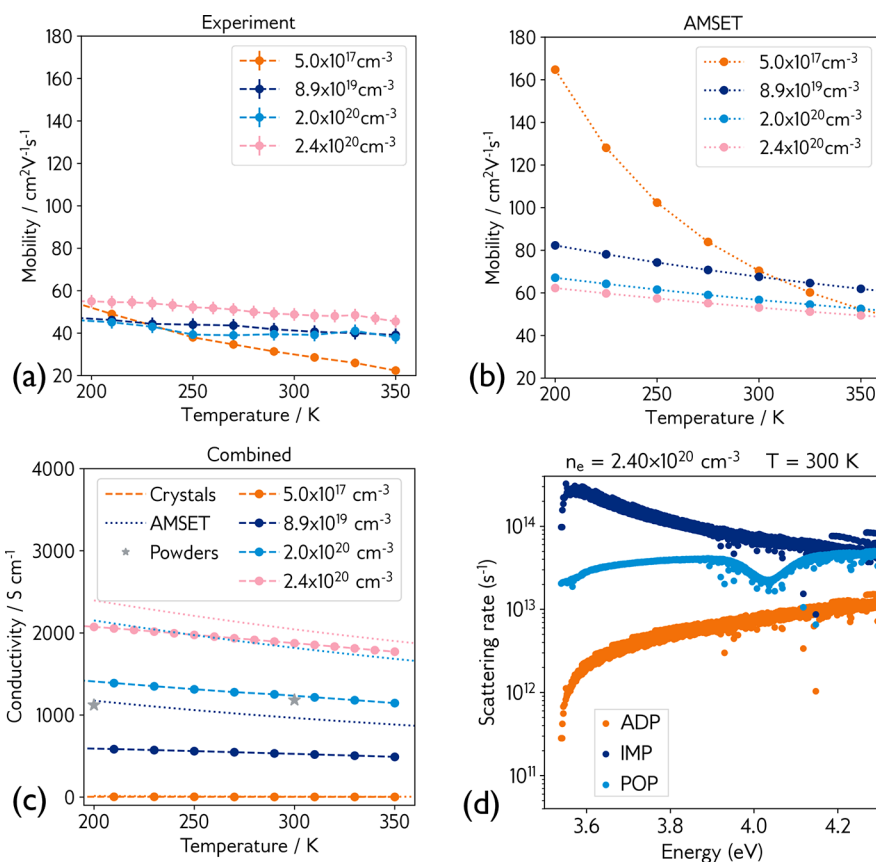


Figure 4. (a) Experimental mobility of undoped and Ga-doped single-crystal ZnSb_2O_6 . (b) Simulated (using AMSET) mobility of ZnSb_2O_6 at carrier concentrations measured from experiment. (c) Single-crystal and simulated conductivity over a range of carrier concentrations, with THz spectroscopy data for an 8% $\text{Zn}_{1-x}\text{Ga}_x\text{Sb}_2\text{O}_6$ solid solution plotted as gray stars. (d) Calculated room-temperature scattering rates at $2.4 \times 10^{20} \text{ cm}^{-3}$. Abbreviations: ADP, acoustic deformation potential scattering; IMP, ionized impurity scattering; and POP, polar optical phonon scattering. Moving from low to high carrier concentrations causes a switch in dominant scattering from POP to IMP.

crystals when doped with increasing Ga content. The presence of adventitious H is the most likely origin of discrepancy, but again we find qualitative agreement with the SCFL analysis. Conductivity rises with increasing carrier concentration and Ga-doping content by several orders of magnitude in the single crystals to 526 S cm^{-1} , 1230 S cm^{-1} , and 1890 S cm^{-1} , respectively, and a similar trend is observed in the powders (conductivity plotted in Figures 4c, S1, and S2), competitive with established TCOs.

Through hard X-ray photoelectron spectroscopy (HAXPES), we find further evidence to support this description of the defect chemistry of ZnSb_2O_6 . At high photon energies (approaching 6 keV), we can exploit the greater photoionization cross-section of Sb 5s states, which from the density-of-states calculation we expect make up the CBM, allowing us to observe any filled conduction band states (more information on the HAXPES results can be found in the SI). Figure 3d shows the HAXPES valence band spectra for undoped and Ga-doped ZnSb_2O_6 aligned to the Fermi level of the doped sample at 0 eV binding energy, with an expanded view ($\times 125$ magnification) provided in the inset between binding energies of 0.75 eV and -0.75 eV. In the undoped sample, there is no photoemission at a binding energy of 0 eV, implying that the conduction band states are unfilled, while the doped sample shows conduction band emission with a typical Fermi–Dirac-like distribution. This is strong evidence of degenerate filling of the conduction band upon Ga-doping,

supporting the prediction of metallic-like conductivity from our defect calculations.

Charge Transport Properties. Charge transport properties are important metrics in assessing the performance of prospective TCOs. Specifically, it is desirable for a TCO to possess high electron mobility in order to maximize conductivity. Figure 4a shows the experimental electron mobility of undoped and Ga-doped ZnSb_2O_6 single crystals over the temperature range 200 to 350 K, where we observed an impressive room-temperature mobility of $49 \text{ cm}^2 \text{ V}^{-1} \text{ s}^{-1}$ at the maximum doping level ($2.4 \times 10^{20} \text{ cm}^{-3}$), resulting in a conductivity of 1890 S cm^{-1} . Our THz domain spectroscopy (TDS) results on powder samples also demonstrate metallic-like conductivity, with a conductivity of 1100 S cm^{-1} achieved at room temperature for $\text{Zn}_{0.92}\text{Ga}_{0.08}\text{Sb}_2\text{O}_6$ (gray stars in Figure 4; the full THz conductivity data set is shown in Figures S1 and S2). Our single crystals display electronic properties that are competitive with those of thin films of ITO, FTO, and AZO, which typically display electron mobilities of $40 \text{ cm}^2 \text{ V}^{-1} \text{ s}^{-1}$ to $60 \text{ cm}^2 \text{ V}^{-1} \text{ s}^{-1}$ and conductivity on the order of $1 \times 10^4 \text{ S cm}^{-1}$.^{2,5,7} In such films, mobility is often limited by ionized impurity scattering, despite the presence of grain boundaries. With suitable deposition conditions and an optimized doping level (sufficiently raising the Fermi level above the conduction band), efficient electron tunneling through grain boundaries can passivate scattering from such defects.³⁹ Polycrystalline ZnSb_2O_6 films may display reduced electron mobility

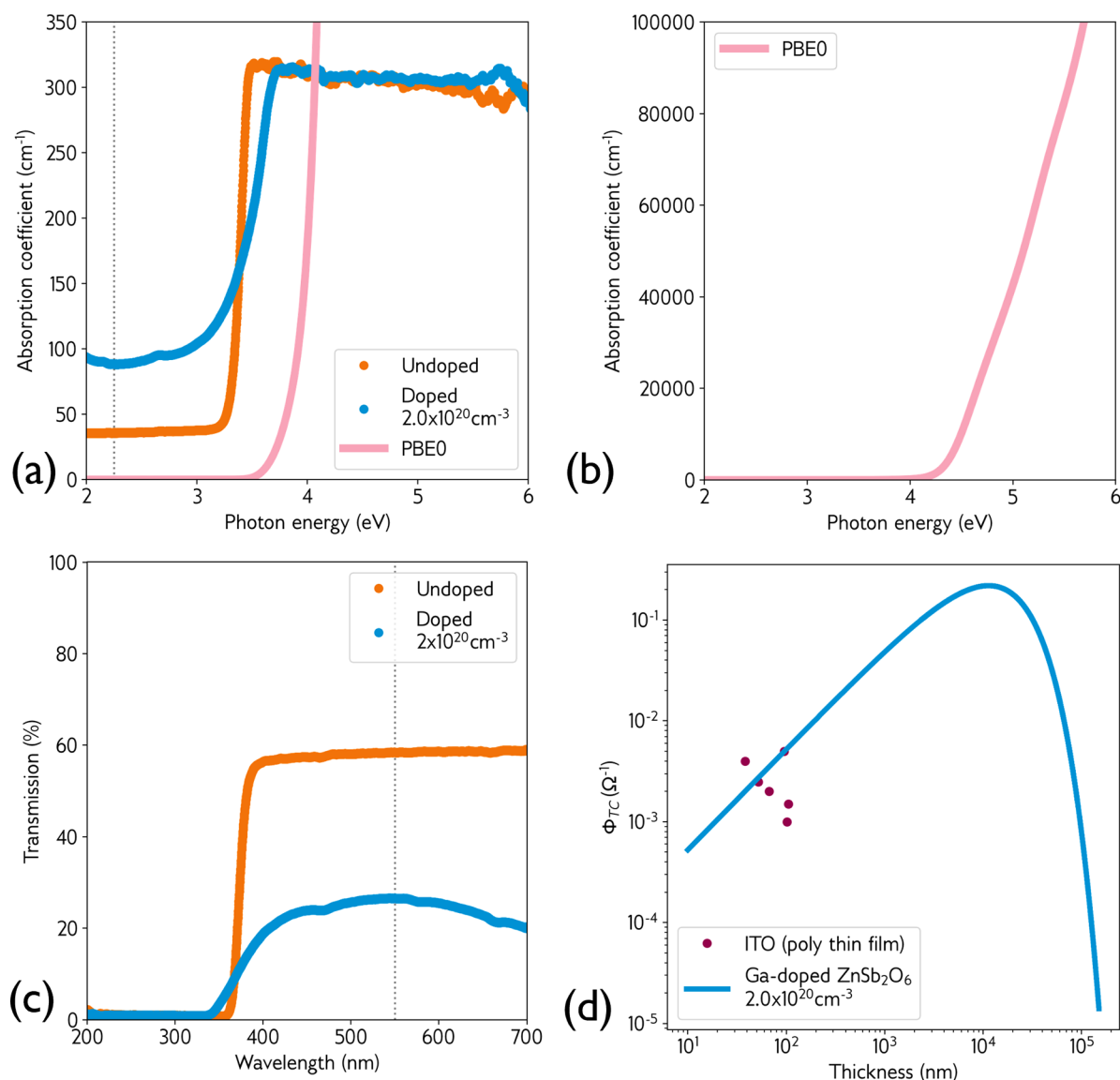


Figure 5. (a) Experimental absorption coefficient of undoped and Ga-doped single crystals, with the calculated PBE0 absorption coefficient (pink) plotted in the same range. (b) Extended plot of the calculated PBE0 absorption coefficient, revealing the much larger value of the optical band gap. (c) Experimental transmission of undoped and Ga-doped single crystals across the visible range. Dotted gray line shows 550 nm on absorption and transmission plot. (d) Haacke figure of merit data at transmittance wavelength of 550 nm, using the doped single-crystal optical data and extracted to different thicknesses, with comparison to data for polycrystalline ITO.⁴¹

compared to our single crystals due to grain boundary scattering, but with an optimized deposition process this mechanism could be suppressed as in the other successful doped TCOs.

To further understand the origin of the high mobility in ZnSb_2O_6 , we performed charge transport calculations using the AMSET package.⁴⁰ This allowed us to calculate the limits to intrinsic mobility from various scattering mechanisms including polar optical phonons (POP), acoustic deformation potentials (ADP), and ionized impurities (IMP). We found that at low carrier concentrations, corresponding to the nominally undoped sample, polar optical phonon scattering dominates, while at higher concentrations the limiting scattering mechanism switches to ionized impurity scattering. This is demonstrated in Figure 4b, where the mobility of the undoped sample displays the strong temperature dependence typically associated with a system dominated by POP scattering, while at high carrier concentrations the mobility

becomes largely temperature independent, indicative of IMP-based scattering. We note that in ZnSb_2O_6 , ADP scattering is largely unimportant, remaining unchanged and at a significantly lower rate than the other mechanisms, regardless of temperature and carrier concentration. In Figure 4d, we explicitly plot the scattering rates at room temperature and high carrier concentration, clearly showing ionized impurity scattering as the dominant scattering mechanism.

There are some discrepancies between the experimental observations and simulations. First, our calculations predict that the nominally undoped material should exhibit a very high electron mobility of around $70 \text{ cm}^2 \text{ V}^{-1} \text{ s}^{-1}$ at room temperature and display a strong temperature dependence. However, our undoped crystal shows the lowest mobility and only a weak temperature dependence. The trend of mobility with increased carrier concentration is in fact unclear across the whole batch of samples. Possible causes of these discrepancies include non-uniform distribution of the dopant during the chemical vapor

transport (CVT) growth process, other unintentional impurities in the samples (perhaps Ca, as observed in the hard X-ray survey spectrum, Figure S3a) that could have detrimental effects on the mobility, or directional dependence effects during measurement of the single crystals—the mobility of ZnSb_2O_6 has reasonable anisotropy, as shown in Figure S7. One other important consideration is that these crystals are very small, only 1 mm^2 , so there is a reasonable error in the measurement. Synthesis of larger single crystals with a refined growth technique could result in improved mobility approaching the value predicted by AMSET; a comparison between calculated and experimental mobility for 24 binary, ternary, and quaternary compounds can be found in ref 40, and is generally reflective of the maturity of the synthesis route. It is also possible that scattering mechanisms not included within the AMSET implementation, such as nonpolar optical phonon scattering, act to lower the experimental mobility and contribute to the discrepancy. Nevertheless, the qualitative agreement between theory and experiment in this study is promising and demonstrates the feasibility and realization of Ga-doped ZnSb_2O_6 as a transparent conducting oxide competitive with industry standard materials.

Optical Properties. Tauc analysis suggests an optical band gap for undoped ZnSb_2O_6 of 3.38 eV, which increases to 3.56 eV upon Ga-doping. This widening of the band gap upon Ga-doping is characteristic of the Moss–Burstein shift that is common among the degenerately doped TCOs. The Tauc-derived band gap for the undoped sample is in remarkably good agreement with the predicted fundamental gap of 3.41 eV from the hQSGW calculation.

In Figure 5a, the absorption coefficient of undoped and Ga-doped ZnSb_2O_6 is plotted over the visible range, along with the calculated PBE0 value. We note that the measured absorption coefficient is below 100 cm^{-1} in both undoped and doped samples at a wavelength of 550 nm, corresponding to the dotted gray line. Further investigation of the computed absorption spectrum revealed a much stronger (several orders of magnitude) absorption onset at around 4.2 eV, shown in Figure 5b. This suggests that the fundamental transition at Γ between the VBM and CBM is forbidden in ZnSb_2O_6 , and that the actual optical band gap could be up to 0.7 eV larger. Experimentally, the thickness of our single crystals prevents us from probing beyond the initial photon absorption peak, causing the plateau at around 300 cm^{-1} . It is known that if sample thickness is too large, transmission can be blocked by a relatively low absorption coefficient beyond the initial onset, as observed in GeSe. In this material, an indirect band gap of around 1.0 eV and absorption coefficient of 150 cm^{-1} are measured in single crystals, and transmission is prevented beyond this energy, while a direct gap of 1.3 eV can be measured in thin films.⁴² Our current calculations predict a large optical band gap of around 4.2 eV, but deposition of thin-film ZnSb_2O_6 is required to ratify the true nature and magnitude of the band gap.

The optical transparency of our $150\text{ }\mu\text{m}$ single crystals can be seen in Figure 1d,e and in the transmission intensity plot in Figure 5c. The undoped crystal is transparent and clear, while the Ga-doped crystal displays a blue tint. The corresponding transmission intensities for the single crystals at a wavelength of 550 nm are 58% and 27%, respectively, denoted by the dotted gray line. Clearly, doping has a detrimental effect on the transparency, which has also been observed in the literature when attempting to dope thin-film ZnSb_2O_6 with F.¹⁸ The

origin of this decrease in transmission is uncertain—we do not observe any mid-gap states from HAXPES that could signify electrons trapped on defect sites in the band gap. The concentration of V_O is not predicted to rise with Fermi level modulation. In contrast, the concentration of Sb_Zn is predicted to decrease—this suggests that neither of these defects is responsible for any loss in transmission. It is possible that transitions from the filled conduction band states to the next-available empty band could cause a mild coloration, as has been investigated in other TCOs.⁴³ Despite this, moving from a thickness of $150\text{ }\mu\text{m}$ to 150 nm by application of the Beer–Lambert law to the 550 nm transmission data for the doped crystal, the transmission is predicted to exceed 99%, suggesting that, at commercially relevant thicknesses, the optical transparency of ZnSb_2O_6 could in fact be superior to that of industry standard ITO.

Finally, we derive the Haacke figure of merit (FOM) for the same Ga-doped crystal, plotted in Figure 5d. This indicates an extremely high FOM at micron thicknesses (approximately $0.2\text{ }\Omega^{-1}$), and values competitive with those of industry standard ITO at thicknesses approaching 100 nm. The development of thin-film ZnSb_2O_6 will allow a more direct comparison of both optical transmission and FOM, rather than using the predicted thin-film transmission intensities.

Band Alignment. Having verified our computational predictions through single-crystal growth and characterization, we investigated the potential of ZnSb_2O_6 as a transparent electrode by calculating its band alignment and comparing to those of existing TCOs, shown in Figure 6. Our calculations

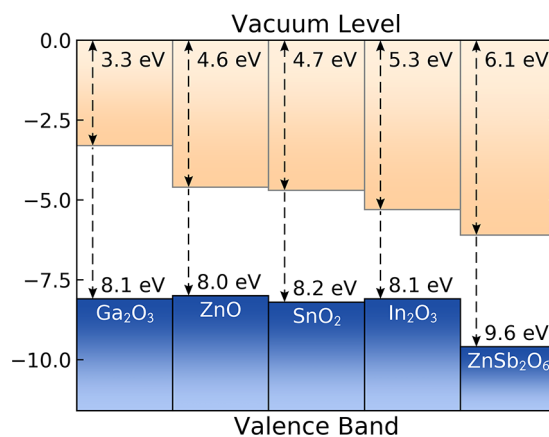


Figure 6. Calculated band alignment of ZnSb_2O_6 compared against common TCOs.^{37,44,45}

reveal an ionization potential (IP) and electron affinity (EA) of 9.6 and 6.1 eV, respectively. Sb 5s states contribute strongly to the CBM, much like *ns* states in the other post-transition metal TCOs, but sit lower in energy due to the increased distance from the nucleus and improved shielding of effective charge by core electrons. Therefore, the EA of ZnSb_2O_6 is significantly greater than that of the industry-leading TCOs. Upon Ga-doping, the Fermi level is predicted to sit above the CBM, which means a work function nearly 1 eV larger than that of In_2O_3 could be achieved. This large work function has tremendous implications in organic photovoltaics (OPVs), which rely entirely on the charge extraction capability of the positive and negative electrodes. A transparent anode with a large electron affinity allows for closer band alignment to low-lying HOMOs (highest occupied molecular orbitals) in OPV

devices, providing better Ohmic contacts, an increase in output voltage, and an enhanced device efficiency.^{46,47} Furthermore, replacing organic hole-extracting layers like PEDOT:PSS with a metal oxide like ZnSb₂O₆ could help to reduce the corrosion on the electrode.⁴⁸ To engineer large work functions in existing TCOs, modulation of the conduction band is required by alloying with heavy, and sometimes toxic, elements (for example, In_{2-x}Tl_xO₃ and Sn_{1-x}Pb_xO₂).^{37,49} Exploiting the native band alignment in ZnSb₂O₆ is a much cheaper, safer, and easier way of incorporating a large work function material into devices.

We have used ab initio calculations to confirm that ZnSb₂O₆ is an earth-abundant transparent conducting oxide, which we have successfully grown in single-crystal form via chemical vapor transport. By studying the intrinsic and extrinsic defect chemistry, we were able to identify an effective doping strategy in order to realize degenerate conductivity through Ga-doping. We have used state-of-the-art packages to predict carrier concentrations and to calculate electron scattering rates, giving a more accurate prediction of charge transport properties that goes beyond the constant relaxation time approximation. Overall, we find good qualitative agreement between these predictions and our single crystals, with our best samples achieving carrier concentrations in excess of $2 \times 10^{20} \text{ cm}^{-3}$, electron mobility up to $49 \text{ cm}^2 \text{ V}^{-1} \text{ s}^{-1}$, and conductivity of 1890 S cm^{-1} . The optical behavior of ZnSb₂O₆ is also promising, with a direct (forbidden) band gap of around 3.4 eV and a wider predicted optical gap up to 4.2 eV, although the slight blue coloration upon Ga-doping requires further investigation. The next logical step is to develop a thin-film deposition process for Ga-doped ZnSb₂O₆, in order to test its performance when incorporated into a device, and to better understand the relationship between charge carrier concentration, transport properties, and optical band gap. Overall, this discovery is a significant milestone in the development of earth-abundant transparent conductors, offering a high-performance alternative to industry standard materials with a unique band edge energy alignment, and opens the door to a whole family of Sb(V)-based transparent conducting oxides.

■ ASSOCIATED CONTENT

Data Availability Statement

Further experimental and computational data can be found at DOI: [10.5281/zenodo.7034578](https://doi.org/10.5281/zenodo.7034578).

Supporting Information

The Supporting Information is available free of charge at <https://pubs.acs.org/doi/10.1021/acsenergylett.2c01961>.

THz spectroscopy, HAXPES survey and core levels, EDS spectra, an extended discussion intrinsic defects, lattice parameters, hQSGW band structure, calculated material properties used for charge transport calculations, directional dependence plots of charge carrier mobility, and Al and F transition level diagrams, including eq S1, Tables S1–S3, and Figures S1–S8 (PDF)

■ AUTHOR INFORMATION

Corresponding Authors

Robin Perry – London Centre for Nanotechnology and Department of Physics and Astronomy, University College London, London WC1E 6BT, U.K.; ISIS Pulsed Neutron and Muon Source, Rutherford Appleton Laboratory, Harwell

Science and Innovation Campus, Didcot, Oxfordshire OX11 0QX, U.K.; Email: robin.perry@ucl.ac.uk

David O. Scanlon – Department of Chemistry, University College London, London WC1H 0AJ, U.K.; Thomas Young Centre, University College London, London WC1E 6BT, U.K.; orcid.org/0000-0001-9174-8601; Email: d.scanlon@ucl.ac.uk

Authors

Adam J. Jackson – Scientific Computing Department, Science and Technology Facilities Council, Rutherford Appleton Laboratory, Harwell Science and Innovation Campus, Didcot, Oxfordshire OX11 0QX, U.K.

Benjamin J. Parrett – London Centre for Nanotechnology and Department of Physics and Astronomy, University College London, London WC1E 6BT, U.K.; Diamond Light Source Ltd., Harwell Science and Innovation Campus, Didcot, Oxfordshire OX11 0DE, U.K.

Joe Willis – Diamond Light Source Ltd., Harwell Science and Innovation Campus, Didcot, Oxfordshire OX11 0DE, U.K.; Department of Chemistry, University College London, London WC1H 0AJ, U.K.; Thomas Young Centre, University College London, London WC1E 6BT, U.K.; orcid.org/0000-0002-1900-2677

Alex M. Ganose – Department of Materials, Imperial College London, London SW7 2AZ, U.K.; orcid.org/0000-0002-4486-3321

W. W. Winnie Leung – Department of Chemistry, University College London, London WC1H 0AJ, U.K.

Yuhan Liu – London Centre for Nanotechnology and Department of Physics and Astronomy, University College London, London WC1E 6BT, U.K.; Department of Chemistry, University College London, London WC1H 0AJ, U.K.

Benjamin A. D. Williamson – Department of Materials Science and Engineering, Norwegian University of Science and Technology, Trondheim 7491, Norway; orcid.org/0000-0002-6242-1121

Timur K. Kim – Diamond Light Source Ltd., Harwell Science and Innovation Campus, Didcot, Oxfordshire OX11 0DE, U.K.; orcid.org/0000-0003-4201-4462

Moritz Hoesch – London Centre for Nanotechnology and Department of Physics and Astronomy, University College London, London WC1E 6BT, U.K.; Diamond Light Source Ltd., Harwell Science and Innovation Campus, Didcot, Oxfordshire OX11 0DE, U.K.; orcid.org/0000-0002-0114-2110

Larissa S. I. Veiga – London Centre for Nanotechnology and Department of Physics and Astronomy, University College London, London WC1E 6BT, U.K.; Diamond Light Source Ltd., Harwell Science and Innovation Campus, Didcot, Oxfordshire OX11 0DE, U.K.

Raman Kalra – Department of Chemistry, University College London, London WC1H 0AJ, U.K.

Jens Neu – Department of Chemistry, Yale University, New Haven, Connecticut 06520-8107, United States; orcid.org/0000-0002-1054-0444

Charles A. Schmuttenmaer – Department of Chemistry, Yale University, New Haven, Connecticut 06520-8107, United States; orcid.org/0000-0001-9992-8578

Tien-Lin Lee – Diamond Light Source Ltd., Harwell Science and Innovation Campus, Didcot, Oxfordshire OX11 0DE, U.K.

Anna Regoutz – Department of Chemistry, University College London, London WC1H 0AJ, U.K.; Diamond Light Source Ltd., Harwell Science and Innovation Campus, Didcot, Oxfordshire OX11 0DE, U.K.; orcid.org/0000-0002-3747-3763

Tung-Chun Lee – Department of Chemistry, University College London, London WC1H 0AJ, U.K.; Institute of Materials Discovery, University College London, London WC1E 7JE, U.K.; orcid.org/0000-0002-3163-0000

Tim D. Veal – Department of Physics and Stephenson Institute for Renewable Energy, University of Liverpool, Liverpool L69 7ZF, U.K.; orcid.org/0000-0002-0610-5626

Robert G. Palgrave – Department of Chemistry, University College London, London WC1H 0AJ, U.K.; orcid.org/0000-0003-4522-2486

Complete contact information is available at:

<https://pubs.acs.org/10.1021/acseenergylett.2c01961>

Author Contributions

[‡]A.J.J., B.J.P., and J.W. contributed equally to this work. DFT calculations were performed by A.J.J., J.W., and A.M.G. with guidance from B.A.D.W. and D.O.S. AMSET calculations were performed by A.M.G. and analyzed by A.M.G. and J.W. Crystal growth and characterization was performed by B.J.P. L.S.I.V. assisted B.J.P. and R.P. performing charge transport measurements. Powder samples were grown and characterized by W.W.W.L. with guidance from R.G.P. and T.-C.L. and assistance from Y.L. Terahertz spectroscopy was performed by W.W.W.L. with assistance from J.N. and C.A.S. Single-crystal optical analysis was performed by T.D.V. HAXPES experiments were performed by B.J.P. and J.W. with guidance from A.R. and T.-L.L. HAXPES data analysis was performed by J.W. with assistance from A.R. T.K.K., M.H., L.S.I.V., R.K., T.-L.L., and A.R. assisted with synchrotron data collection throughout the project. The manuscript was written and prepared by J.W. with input from all authors. Crystal growth and characterization was managed by R.P. Computational work was managed by D.O.S. The overall project was conceived by D.O.S.

Notes

The authors declare no competing financial interest.

[†]Deceased, July 26, 2020.

ACKNOWLEDGMENTS

This work used the ARCHER and ARCHER2 UK National Supercomputing Service (<https://www.archer2.ac.uk>), via our membership of the UK's HEC Materials Chemistry Consortium, which is funded by the EPSRC (EP/L000202, EP/R029431, and EP/T022213). We are grateful to the UK Materials and Molecular Modelling Hub for computational resources (Thomas and Young), which is partially funded by the EPSRC (EP/P020194/1 and EP/T022213/1). The authors acknowledge the use of the UCL Legion, Myriad, Kathleen, and Thomas High Performance Computing Facilities (Legion@UCL, Myriad@UCL, Kathleen@UCL, Thomas@UCL), and associated support services, in the completion of this work. We acknowledge Diamond Light Source for access to beamline I09 under proposal number SI24449-1. J.W. and D.O.S. acknowledge Diamond Light Source for co-sponsorship of an Eng.D. studentship on the EPSRC Centre for Doctoral Training in Molecular Modelling and Materials Science (EP/L015862/1). A.J.J. and D.O.S.

acknowledge support for the EPSRC (grant number EP/N01572X/1). W.W.W.L. acknowledges a Royal Society of Chemistry Researcher Mobility Grant. The authors thank Gavin Stenning at the ISIS material characterization lab for use of XRD and Quantum Design PPMS. We acknowledge useful discussions with Dr. John Buckeridge and Dr. Christopher N. Savory.

REFERENCES

- (1) Granqvist, C.; Hultåker, A. Transparent and conducting ITO films: new developments and applications. *Thin Solid Films* **2002**, *411*, 1–5.
- (2) Swallow, J. E. N.; Williamson, B. A. D.; Whittles, T. J.; Birkett, M.; Featherstone, T. J.; Peng, N.; Abbott, A.; Farnworth, M.; Cheatham, K. J.; Warren, P.; Scanlon, D. O.; Dhanak, V. R.; Veal, T. D. Self-Compensation in Transparent Conducting F-Doped SnO₂. *Adv. Funct. Mater.* **2018**, *28*, 1701900.
- (3) Li, J.; Sathasivam, S.; Taylor, A.; Carmalt, C. J.; Parkin, I. P. Single step route to highly transparent, conductive and hazy aluminium doped zinc oxide films. *RSC Adv.* **2018**, *8*, 42300–42307.
- (4) Bhachu, D. S.; Scanlon, D. O.; Sankar, G.; Veal, T. D.; Egdell, R. G.; Cibin, G.; Dent, A. J.; Knapp, C. E.; Carmalt, C. J.; Parkin, I. P. Origin of High Mobility in Molybdenum-Doped Indium Oxide. *Chem. Mater.* **2015**, *27*, 2788–2796.
- (5) Swallow, J. E. N.; et al. Resonant doping for high mobility transparent conductors: the case of Mo-doped In₂O₃. *Materials Horizons* **2020**, *7*, 236–243.
- (6) Koida, T.; Ueno, Y.; Shibata, H. In₂O₃-Based Transparent Conducting Oxide Films with High Electron Mobility Fabricated at Low Process Temperatures. *Physica Status Solidi (A)* **2018**, *215*, 1700506.
- (7) Dixon, S. C.; Sathasivam, S.; Williamson, B. A. D.; Scanlon, D. O.; Carmalt, C. J.; Parkin, I. P. Transparent conducting n-type ZnO:Sc – synthesis, optoelectronic properties and theoretical insight. *J. Mater. Chem. C* **2017**, *5*, 7585–7597.
- (8) Williamson, B. A. D.; et al. Resonant Ta Doping for Enhanced Mobility in Transparent Conducting SnO₂. *Chem. Mater.* **2020**, *32*, 1964–1973.
- (9) Zhang, L.; Zhou, Y.; Guo, L.; Zhao, W.; Barnes, A.; Zhang, H.-T.; Eaton, C.; Zheng, Y.; Brahlek, M.; Haneef, H. F.; Podraza, N. J.; Chan, M. H. W.; Gopalan, V.; Rabe, K. M.; Engel-Herbert, R. Correlated metals as transparent conductors. *Nat. Mater.* **2016**, *15*, 204–210.
- (10) Kim, H. J.; Kim, U.; Kim, H. M.; Kim, T. H.; Mun, H. S.; Jeon, B.-G.; Hong, K. T.; Lee, W.-J.; Ju, C.; Kim, K. H.; Char, K. High Mobility in a Stable Transparent Perovskite Oxide. *Appl. Phys. Express* **2012**, *5*, 061102.
- (11) Janowitz, C.; Scherer, V.; Mohamed, M.; Krapf, A.; Dwelk, H.; Manzke, R.; Galazka, Z.; Uecker, R.; Irmischer, K.; Fornari, R.; Michling, M.; Schmeißer, D.; Weber, J. R.; Varley, J. B.; Van de Walle, C. G. Experimental electronic structure of In₂O₃ and Ga₂O₃. *New J. Phys.* **2011**, *13*, 085014.
- (12) Shannon, R.; Gillson, J.; Bouchard, R. Single crystal synthesis and electrical properties of CdSnO₃, Cd₂SnO₄, In₂TeO₆ and CdIn₂O₄. *J. Phys. Chem. Solids* **1977**, *38*, 877–881.
- (13) Mizoguchi, H.; Woodward, P. M. Electronic Structure Studies of Main Group Oxides Possessing Edge-Sharing Octahedra: Implications for the Design of Transparent Conducting Oxides. *Chem. Mater.* **2004**, *16*, 5233–5248.
- (14) Hautier, G.; Miglio, A.; Waroquiers, D.; Rignanese, G.-M.; Gonze, X. How Does Chemistry Influence Electron Effective Mass in Oxides? A High-Throughput Computational Analysis. *Chem. Mater.* **2014**, *26*, 5447–5458.
- (15) Kikuchi, N.; Hosono, H.; Kawazoe, H.; Tanegashima, O.; Ota, I.; Kimura, Y. Carrier Generation in Wide-Gap Conductor, Zinc Antimonate. *J. Am. Ceram. Soc.* **2005**, *88*, 2793–2797.

- (16) Tamaki, J.; Yamada, Y.; Yamamoto, Y.; Matsuoka, M.; Ota, I. Sensing properties to dilute hydrogen sulfide of ZnSb₂O₆ thick-film prepared by dip-coating method. *Sens. Actuators, B* **2000**, *66*, 70–73.
- (17) Zhu, B.; Xie, C.; Wang, A.; Zeng, D.; Hu, M.; Wang, W. Electrical conductivity and gas sensitivity of Zn–Sb–O thick films. *Mater. Res. Bull.* **2004**, *39*, 409–415.
- (18) Potter, D. *Zinc-based thin films for transparent conducting oxide applications*. Ph.D. thesis, University College London, 2018.
- (19) Li, J.; Du, K.; Lai, Y.; Chen, Y.; Zhang, Z. ZnSb₂O₆: an advanced anode material for Li-ion batteries. *J. Mater. Chem. A* **2017**, *5*, 10843–10848.
- (20) U.S. Geological Survey: *Mineral commodity summaries 2022*; U.S. Geological Survey 2022; p 202.
- (21) Zhang, G.-X.; Reilly, A. M.; Tkatchenko, A.; Scheffler, M. Performance of various density-functional approximations for cohesive properties of 64 bulk solids. *New J. Phys.* **2018**, *20*, 063020.
- (22) Momma, K.; Izumi, F. VESTA: a three-dimensional visualization system for electronic and structural analysis. *J. Appl. Crystallogr.* **2008**, *41*, 653–658.
- (23) Shannon, R. D. Revised effective ionic radii and systematic studies of interatomic distances in halides and chalcogenides. *Acta Crystallogr., Sect. A* **1976**, *32*, 751–767.
- (24) Toby, B. H.; Von Dreele, R. B. GSAS-II: the genesis of a modern open-source all purpose crystallography software package. *J. Appl. Crystallogr.* **2013**, *46*, S44–S49.
- (25) Lebens-Higgins, Z.; Scanlon, D.; Paik, H.; Sallis, S.; Nie, Y.; Uchida, M.; Quackenbush, N.; Wahila, M.; Sterbinsky, G.; Arena, D. A.; Woicik, J.; Schlom, D.; Piper, L. Direct Observation of Electrostatically Driven Band Gap Renormalization in a Degenerate Perovskite Transparent Conducting Oxide. *Phys. Rev. Lett.* **2016**, *116*, 027602.
- (26) Walsh, A.; Da Silva, J. L. F.; Wei, S.-H.; Korber, C.; Klein, A.; Piper, L. F. J.; DeMasi, A.; Smith, K. E.; Panaccione, G.; Torelli, P.; Payne, D. J.; Bourlange, A.; Egdell, R. G. Nature of the Band Gap of In₂O₃. Revealed by First-Principles Calculations and X-Ray Spectroscopy. *Phys. Rev. Lett.* **2008**, *100*, 167402.
- (27) Jackson, A. J.; Ganose, A. M.; Regoutz, A.; Egdell, R. G.; Scanlon, D. O. Galore: Broadening and weighting for simulation of photoelectron spectroscopy. *J. Open Source Software* **2018**, *3*, 773.
- (28) Yeh, J.; Lindau, I. Atomic subshell photoionization cross sections and asymmetry parameters: Z1–103. *Atomic Data and Nuclear Data Tables* **1985**, *32*, 1–155.
- (29) Oba, F.; Togo, A.; Tanaka, I.; Paier, J.; Kresse, G. Defect energetics in ZnO: A hybrid Hartree-Fock density functional study. *Phys. Rev. B* **2008**, *77*, 245202.
- (30) Vasheghani Farahani, S. K.; Veal, T. D.; Mudd, J. J.; Scanlon, D. O.; Watson, G. W.; Bierwagen, O.; White, M. E.; Speck, J. S.; McConville, C. F. Valence-band density of states and surface electron accumulation in epitaxial SnO₂ films. *Phys. Rev. B* **2014**, *90*, 155413.
- (31) Buckeridge, J.; Scanlon, D.; Walsh, A.; Catlow, C. Automated procedure to determine the thermodynamic stability of a material and the range of chemical potentials necessary for its formation relative to competing phases and compounds. *Comput. Phys. Commun.* **2014**, *185*, 330–338.
- (32) Mott, N. F. Metal-Insulator Transition. *Rev. Mod. Phys.* **1968**, *40*, 677–683.
- (33) Edwards, P. P.; Sienko, M. J. Universality aspects of the metal-nonmetal transition in condensed media. *Phys. Rev. B* **1978**, *17*, 2575.
- (34) Scanlon, D. O.; Kehoe, A. B.; Watson, G. W.; Jones, M. O.; David, W. I. F.; Payne, D. J.; Egdell, R. G.; Edwards, P. P.; Walsh, A. Nature of the Band Gap and Origin of the Conductivity of PbO₂ Revealed by Theory and Experiment. *Phys. Rev. Lett.* **2011**, *107*, 246402.
- (35) Spooner, K. B.; Ganose, A. M.; Scanlon, D. O. Assessing the limitations of transparent conducting oxides as thermoelectrics. *J. Mater. Chem. A* **2020**, *8*, 11948–11957.
- (36) Chatratin, I.; Sabino, F. P.; Reunchan, P.; Limpijumngong, S.; Varley, J. B.; Van de Walle, C. G.; Janotti, A. Role of point defects in the electrical and optical properties of In₂O₃. *Phys. Rev. Mater.* **2019**, *3*, 074604.
- (37) Scanlon, D. O.; Watson, G. W. On the possibility of p-type SnO₂. *J. Mater. Chem.* **2012**, *22*, 25236.
- (38) Janotti, A.; Van de Walle, C. G. Native point defects in ZnO. *Phys. Rev. B* **2007**, *76*, 165202.
- (39) Nguyen, V. H.; Gottlieb, U.; Valla, A.; Muñoz, D.; Bellet, D.; Muñoz-Rojas, D. Electron tunneling through grain boundaries in transparent conductive oxides and implications for electrical conductivity: the case of ZnO:Al thin films. *Materials Horizons* **2018**, *5*, 715–726.
- (40) Ganose, A. M.; Park, J.; Faghaninia, A.; Woods-Robinson, R.; Persson, K. A.; Jain, A. Efficient calculation of carrier scattering rates from first principles. *Nat. Commun.* **2021**, *12*, 2222.
- (41) Ellmer, K. Past achievements and future challenges in the development of optically transparent electrodes. *Nat. Photonics* **2012**, *6*, 809–817.
- (42) Murgatroyd, P. A. E.; Smiles, M. J.; Savory, C. N.; Shalvey, T. P.; Swallow, J. E. N.; Fleck, N.; Robertson, C. M.; Jäckel, F.; Alaria, J.; Major, J. D.; Scanlon, D. O.; Veal, T. D. GeSe: Optical Spectroscopy and Theoretical Study of a van der Waals Solar Absorber. *Chem. Mater.* **2020**, *32*, 3245–3253.
- (43) Ha, V.-A.; Waroquiers, D.; Rignanese, G.-M.; Hautier, G. Influence of the second gap on the transparency of transparent conducting oxides: An ab initio study. *Appl. Phys. Lett.* **2016**, *108*, 201902.
- (44) Zhang, J.; Willis, J.; Yang, Z.; Lian, X.; Chen, W.; Wang, L.-S.; Xu, X.; Lee, T.-L.; Chen, L.; Scanlon, D. O.; Zhang, K. H. Deep UV transparent conductive oxide thin films realized through degenerately doped wide-bandgap gallium oxide. *Cell Rep. Phys. Sci.* **2022**, *3*, 100801.
- (45) Höffling, B.; Schleife, A.; Rödl, C.; Bechstedt, F. Band discontinuities at Si-TCO interfaces from quasiparticle calculations: Comparison of two alignment approaches. *Phys. Rev. B* **2012**, *85*, 035305.
- (46) Greiner, M. T.; Lu, Z.-H. Thin-film metal oxides in organic semiconductor devices: their electronic structures, work functions and interfaces. *NPG Asia Materials* **2013**, *5*, e55–e55a.
- (47) Cao, W.; Xue, J. Recent progress in organic photovoltaics: device architecture and optical design. *Energy Environ. Sci.* **2014**, *7*, 2123.
- (48) Kim, S.; Saeed, M. A.; Kim, S. H.; Shim, J. W. Enhanced hole selecting behavior of WO₃ interlayers for efficient indoor organic photovoltaics with high fill-factor. *Appl. Surf. Sci.* **2020**, *527*, 146840.
- (49) Ganose, A. M.; Scanlon, D. O. Band gap and work function tailoring of SnO₂ for improved transparent conducting ability in photovoltaics. *J. Mater. Chem. C* **2016**, *4*, 1467–1475.